

Integrated pulsed optically pumped Rb atomic clock with frequency stability of 10^{-15}

Qiang Hao^{1,2,*}, Shaojie Yang,¹ Jun Ruan,^{1,2} Peter Yun,^{1,2} and Shougang Zhang^{1,2,†}

¹*National Time Service Center, Chinese Academy of Sciences, Xi'an 710600, China*

²*University of Chinese Academy of Sciences, Beijing 100049, China*



(Received 29 August 2023; revised 13 November 2023; accepted 18 January 2024; published 1 February 2024)

Pulsed optically pumped (POP) Rb atomic clock is considered to be a powerful technique for the Rb atomic clock due to the capability of light-shift mitigation and atomic spectroscopy narrowing. Relevant investigations are conducted over two decades, however, no integrated prototype of such a kind of clock has been reported yet. Here, we present an integrated prototype of the POP Rb atomic clock and quantitatively characterize its physical properties. The atomic clock shows a short-term fractional frequency stability of $2.6 \times 10^{-13}/\sqrt{\tau}$ (where τ is the averaging time), and comes to 2.3×10^{-15} with 40 000 s averaging (drift removed) under atmospheric conditions. Physical effects contributing to the long-term frequency stability are carefully analyzed and cavity-pulling shift is identified as the leading limit. The techniques presented here enable realizing a low 10^{-15} level vapor-cell atomic clock under atmospheric conditions, which could benefit a wide range of terrestrial applications, such as quantum communication, decimeter-level terrestrial positioning.

DOI: [10.1103/PhysRevApplied.21.024003](https://doi.org/10.1103/PhysRevApplied.21.024003)

I. INTRODUCTION

Technologies including quantum communication [1], gravitational-wave detection [2], low-Earth-orbit satellite navigation [3] and decimeter-level terrestrial positioning [4], require subnanosecond synchronization, a precision level beyond what the global navigation satellite system (GNSS) can provide. To address this challenge, one of the practical solutions is to deploy local atomic clocks in the networks. These large-scale infrastructures require numeric technical and physical indicators to atomic clocks, including precision and size, weight, power, and cost, which rules out bulky and expensive alternatives, such as hydrogen atomic clocks [5], cold atomic clocks [6–8], and optical clocks [9,10]. Therefore, compact atomic clocks based on coherent population trapping [11,12], two-photon transition [13], cooled ions [14,15], etc., have been proposed. Among them, the pulsed optically pumped (POP) Rb clock is considered a promising option due to the potential for accessing the short-term stability of active hydrogen maser in small size [16].

In 1964, the separated oscillation field technique was employed in the Rb atomic clock to eliminate light shift and narrow the clock signal [17]. Because it is difficult to obtain fast and stable light pulses through the discharge lamp, the atomic clock did not work well at that time.

With the maturity of semiconductor lasers and acousto-optic modulators, the separated oscillation field technique was successfully applied to the Rb atomic clock, known as the POP Rb atomic clock, in 2004 [18]. In 2012, Instituto Nazionale di Ricerca Metrologica (INRIM) reported a POP Rb clock with a short-term stability of $1.7 \times 10^{-13}/\sqrt{\tau}$ (1–400 s) and 5×10^{-15} at 4000 s [19]. Meanwhile, several groups are conducting relevant studies to push the development of POP Rb clocks [20–25].

Recently, INRIM, in collaboration with Leonardo S.p.A., demonstrated a POP Rb clock for space applications, exhibiting a frequency stability of 1.2×10^{-13} at 1 s and achieved the value of 6×10^{-16} for integration time of 40 000 s (drift removed) [26]. The performance was achieved on a tabletop platform and the physics package was placed in a vacuum chamber. In contrast, to develop a cheap and high-performance atomic clock for terrestrial applications, we demonstrate an integrated prototype of the POP Rb atomic clock in 23 l. In order to decrease the sensitivity of the physics package, we reduce the buffer-gas pressure in the absorption cell, seal the physics package at standard atmospheric pressure, and adopt a magnetron-type microwave cavity to shrink the size of the physics package. The prototype shows a frequency stability of 2.3×10^{-15} (drift removed) under atmospheric conditions, whose noise levels are much higher than under vacuum [24,26,27].

This paper is organized as follows: Section II introduces the design of the integrated POP Rb atomic clock.

*Corresponding author. haoq@ntsc.ac.cn

†Corresponding author. zhangs@ntsc.ac.cn

Section III gives a detailed analysis of the characteristics of the clock, including atoms decay in buffer gases, clock signal, and performance. Section IV analyzes the main contributors to the long-term frequency stability. Section V concludes the results and presents a discussion.

II. ATOMIC CLOCK SCHEME

Figure 1(a) shows a schematic of the proposed POP Rb atomic clock. It mainly consists of four parts: physics package, laser bench, frequency synthesizer, and data-acquisition module. As plotted in Fig. 1(b), the absorption cell at the center of the figure is used to generate clock signal, which is filled with ^{87}Rb atoms vapor and Ar/N₂ gas mixture (pressure ratio $P_{\text{Ar}}/P_{\text{N}_2} = 1.6$). The absorption cell, with 2 cm in both length and diameter, is placed in a magnetron-type microwave cavity. The microwave cavity has an external diameter of 3.3 cm and an axial length of 3.5 cm. It shows TE₀₁₁-like resonant mode [28]. The resonant frequency and quality factor are 6.835 GHz and 140, respectively. The cavity-cell assembly is enclosed in two layers of magnetic shields. A plane-convex lens with 5-cm focal length is used to concentrate the transmitted light. To reduce the impact of thermal convection and barometric effects, the physics package is hermetically sealed at standard atmospheric pressure [29].

The buffer-gas collision shift for microwave [30] or optical transition [31] is given as

$$\Delta\nu(P, \Delta T) = P(\beta' + \delta'\Delta T + \gamma'\Delta T^2), \quad (1)$$

where P is gas pressure, β' the pressure frequency-shift coefficient, δ' and γ' the linear and quadratic temperature coefficients, ΔT the difference between the operating temperature and reference temperature. To decrease the temperature sensitivity of the physics package, we decrease the buffer-gas pressure to 15 Torr in contrast to the commonly

used pressure of 25 Torr [24–26]. The physics package temperature sensitivity could decrease 40% through buffer-gas pressure reduction, according to Eq. (1). As shown in Fig. 3, the optical frequency is shifted about 100 MHz by buffer-gas collision, which is compensated by the AOM. The microwave transition frequency is shifted by about 2.8 kHz.

The optical bench employs a distributed feedback (DFB) laser diode at 780.24 nm with 70-mW power. After the optical isolator, a nonpolarized beam splitter divides about 2-mW power for saturated absorption frequency stabilization. The reference cell for laser-frequency stabilization contains only ^{87}Rb atom vapor, which is surrounded by one layer of magnetic shielding. The length and diameter of the reference cell are 5 and 2 cm, respectively. The major beam then singly passes through a 100-MHz acousto-optic modulator (AOM), which acts as an optical switch with 30-dB power extinction ratio. The first-order diffracted beam is raised to 75 mm by a beam elevator to keep coaxial with the physics package. Before entering the physics package, the diameter of the laser beam is expanded to 10 mm. To decrease the temperature sensitivity of the optical bench, the temperatures of AOM and reference cell are separately controlled at 301 and 303 K with the fluctuation less than 10 mK. Two identical optical benches are built to characterize frequency noise of the laser. Figure 2 shows the beatnote between the benches, indicating a 3-dB bandwidth of 2.8 MHz.

A microwave synthesizer is used to generate the 6.835-GHz signal and an AOM driving signal. The 6.835-GHz signal is produced by the frequency mixing of a 6.8-GHz phase-locked dielectric resonant oscillator (PLDRO) and a direct digital synthesizer (DDS), both are referred to a common quartz oscillator [32]. The microwave frequency and power are changed by the DDS and a voltage control attenuator, respectively. A power divider and detector are connected to the microwave output to monitor the output

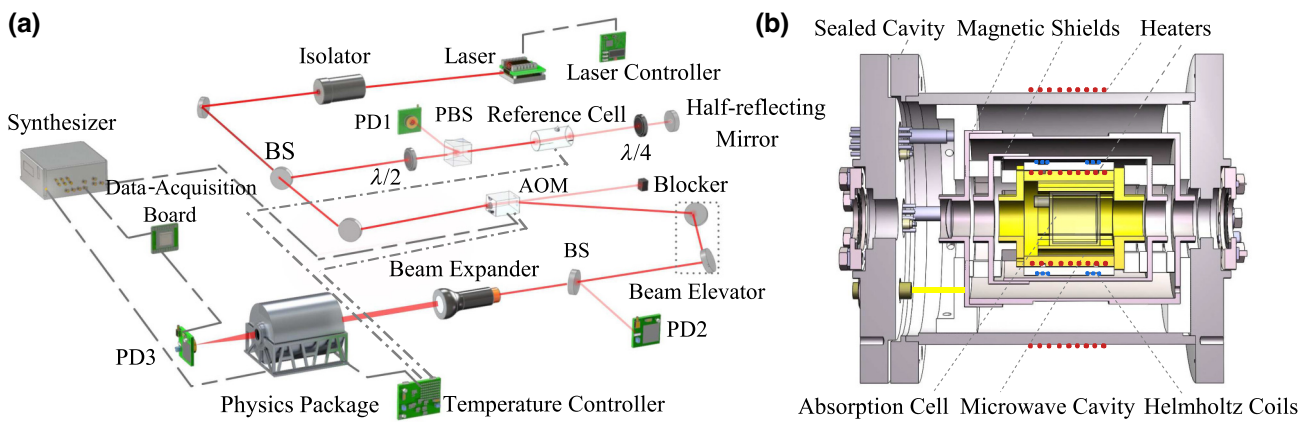


FIG. 1. Schematic diagram of the POP Rb atomic clock: PD, photodetector; BS, beam splitter; PBS, polarizing beam splitter; AOM, acousto-optic modulator.

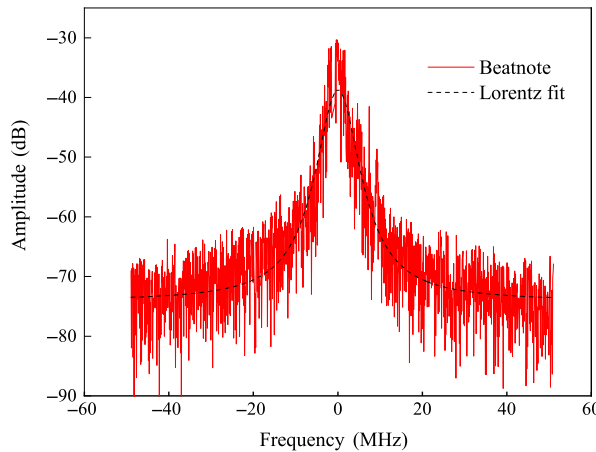


FIG. 2. A beatnote between two identical optical benches, whose frequencies are stabilized by the saturated absorption spectrum.

power. The microwave phase noise at harmonic frequencies of the clock interrogation frequency (213 Hz in our case) may decrease the signal-to-noise ratio [33]. We measured the absolute phase noise of the 6.835-GHz signal. It is fitted as $L(f) = 10^{-8.05} \times f^{-1.15} \text{ Hz}^{-1}$ ($100 \text{ Hz} \leq f \leq 1000 \text{ Hz}$), leading to a Dick effect contribution less than $5 \times 10^{-14}/\sqrt{\tau}$.

A programmable data-acquisition board is also embedded in our prototype for servo control. Four 16-bit DACs are employed to generate the pulse sequence and three 16-bit ADCs are employed to monitor the clock signal, laser power, and microwave power. A 20-bit DAC is used to control the frequency of the quartz oscillator. All the DACs and ADCs are managed by a field programmable gate array (FPGA). The clock operating sequence is periodically arranged as follows: the total cycle period T_c is

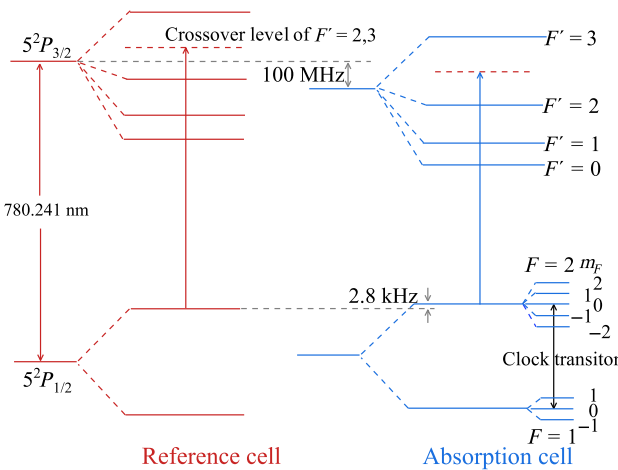


FIG. 3. Energy diagram of the ^{87}Rb atom, the fine-structure and hyperfine-structure energy levels in the absorption cell are shifted by 100 MHz and 2.8 kHz through buffer-gas collision.

4.7 ms, the pump pulse for quantum state preparation is 0.4 ms, two separate microwave pulses are 0.4 ms, the free-evolution time is 3.3 ms, the probe pulse is 0.2 ms.

The configuration of pulse timing is based on the optimization of short-term stability. The free evolution time is mainly limited by the coherent relaxation time T_2 of the thermal Rb atoms. T_2 is measured to be 3.63 ms in our case. We optimized pulse timing according to the relationship $T_f + T_d \approx T_2$ [19]. If $T_f + T_d > T_2$, the central Ramsey fringe will be narrower and the duty cycle will increase, but the signal-to-noise ratio will decrease due to the decoherence of the atom ensemble. If $T_f + T_d < T_2$, the short-term stability will deteriorate because of the increasing contribution of laser noises and microwave phase noise.

The clock prototype is designed to operate under atmospheric conditions. Due to ambient temperature greatly affecting the clock frequency through buffer-gas collision, laser-power fluctuation, and other factors, we integrate five temperature controllers in the prototype. Among them, two channels are used to stabilize the absorption cell temperature, which is set on the external surface of the microwave cavity and sealed cavity. The remaining channels are used to control the temperatures of the laser diode, AOM and reference cell, respectively. Additionally, the prototype is placed on a homemade baseplate for fast heat dissipation, which is cooled to 292 K by thermoelectric coolers (TECs).

III. ATOMIC CLOCK CHARACTERISTICS

Rb atomic clock works on the thermal atomic vapor contained in a glass cell, so the Doppler broadening and relaxation arising from collision with the bare glass surface have a strong impact on the SNR and linewidth of the clock signal. Buffer gases are used to ensure atomic mean free path less than the wavelength of the microwave radiation [34]. Whereas, they also bring in buffer-gas collision relaxation.

A. Atom relaxation in buffer gases

In vapor-cell atomic clocks, the Rb atoms relaxation is mainly caused by spin exchange, diffusion relaxation, and buffer-gas collision [35]. We assume an equal decay rate for all Zeeman sublevels due to buffer-gas collision-induced decay [36], the population relaxation time T_1 of the Zeeman sublevel $|F = 1, m_f = 0\rangle$ is characterized by the Franzen method [37]. Figure 4 shows the optical-density variation as a function of the dark time, and the parameters are well described by the exponential decay with a time constant of 2.79 (0.03) ms.

Additionally, we use Ramsey spectroscopy to measure the coherent relaxation time T_2 , which affects the off-diagonal elements of the density matrix. Figure 5 presents the contrast of the central Ramsey fringe (C) versus free-evolution time T_f , and we extract $T_2 = 3.63$ (0.07) ms

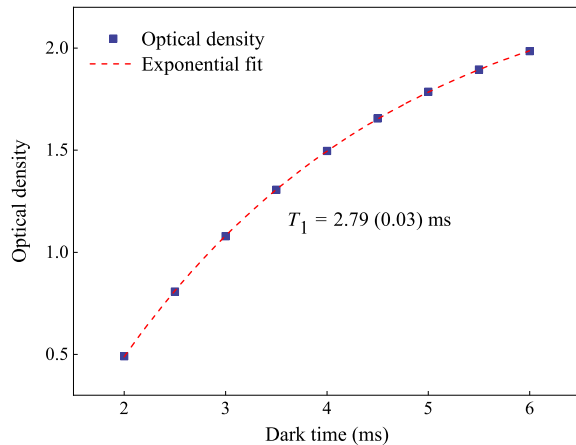


FIG. 4. Optical-density variation as a function of dark time (purple squares) is fitted with an exponential decay (red dashed line), the optical density is $-\ln(I_t/I_0)$, I_t , and I_0 represent the transmitted and incident optical power, respectively.

from the relationship $C(T_f) = C_0 \exp(-T_f/T_2)$, where C_0 is a constant [38]. Since microwave pulse duration (T_μ) affects the measurement result of T_2 , T_f ranges from 4.5 to 8.5 ms to ensure $T_\mu \ll T_f$.

B. Clock signal

An equivalent three-level system is used to describe the atomic ensemble interacting with laser and microwave, which is composed of two clock levels ($|F=1, m_f=0\rangle$ and $|F=2, m_f=0\rangle$) and excited state ($5^2P_{3/2}$), see Fig. 3. The population inversion Δ and coherence δ_{12} of the hyperfine levels, in the formalism of the density matrix, are approximately given by

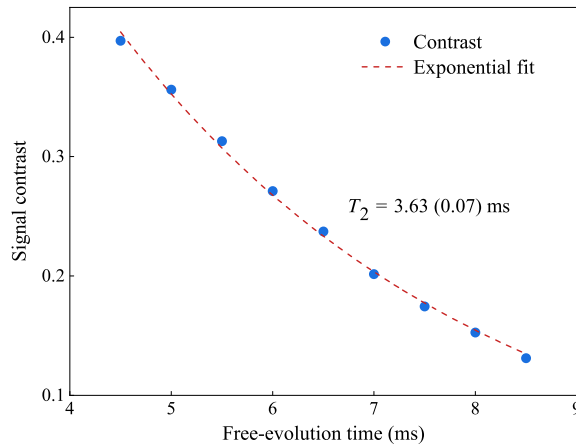


FIG. 5. Contrast of the central Ramsey fringe as a function of free-evolution time in blue circles, indicating the decoherence rate of $T_2 = 3.63 (0.07) \text{ ms}$ by exponential fitting (red dashed line).

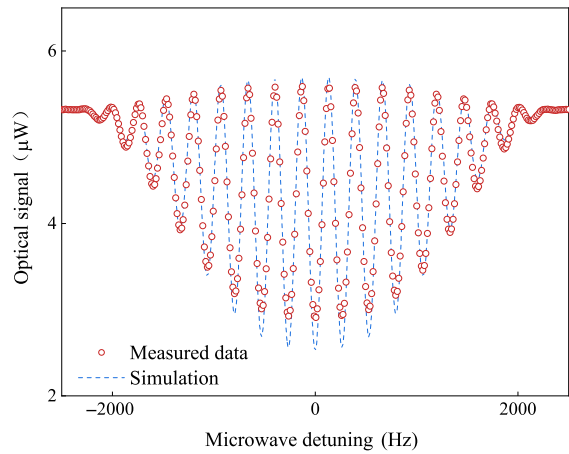


FIG. 6. Clock signal as a function of microwave detuning, where the free-evolution time T_f is 3.3 ms and the central fringe has a linewidth of 149 Hz, consistent well with theoretical value $1/(2T_f)$.

$$\dot{\Delta} + (1/T_1 + \Gamma_p)\Delta = 2b\text{Re}(\delta_{12}) + \Gamma_p, \quad (2)$$

$$\dot{\delta}_{12} + (1/T_2 + \Gamma_p + i\Omega_\mu)\delta_{12} = -i\frac{b}{2}\Delta, \quad (3)$$

where $\Delta = \rho_{22} - \rho_{11}$, ρ_{11} , and ρ_{22} the population of state $|F=1, m_f=0\rangle$ and $|F=2, m_f=0\rangle$, Γ_p the optical pumping rate, Ω_μ is microwave frequency detuning, b is the microwave Rabi frequency [18,39].

Given that the atom-microwave and atom-light interaction occur in separate time, the above equations are numerically solved in each interaction phase using the measured parameters T_1 and T_2 . The atom clock signal is experimentally measured by optical absorption method. Figure 6 plots the calculated and measured Ramsey fringes. It is interesting to observe that both experimental and measured results show a similar convex shape in the Rabi envelopes, indicating effective measurement of the atom relaxation rates [39]. The discrepancy between theory and experiment is due to the nonuniform distribution of light and microwave [40].

The shot-noise contribution to the short-term frequency stability is [19]

$$\sigma(\tau) = \frac{\Delta\nu}{\pi v_0 C \sqrt{\eta N}} \sqrt{\frac{T_c}{\tau}}, \quad (4)$$

where v_0 is the clock-transition frequency, $\Delta\nu$ the linewidth of the central Ramsey fringe, η the efficiency of the photodetector, N the photon number detected by the photodetector. In Fig. 6, the linewidth and contrast of the central fringe are 149 Hz and 51%, respectively, corresponding to the shot-noise limit of $1.9 \times 10^{-14}/\sqrt{\tau}$.

C. Frequency stability

Figure 7 shows the photograph of the POP Rb clock, whose volume and power consumption are 23 l and 45



FIG. 7. Photograph of the atomic clock prototype, the size is 18 cm (height) \times 28 cm (width) \times 45 cm (length).

W, respectively. To verify the performance of the developed atomic clock, we measure the fractional frequency over 48 h against a hydrogen maser. The resulting frequency stability is presented in Fig. 8, which scales as $2.6 \times 10^{-13}/\sqrt{\tau}$ at averaging times 1–400 s. It is consistent with white-frequency noise behavior, which arises from the frequency and intensity noise of the optical bench [25]. The frequency stability reaches 2.3×10^{-15} at averaging time of 40 000 s (a linear drift of $2.2 \times 10^{-13}/\text{day}$ removed), which is mainly limited by cavity-pulling shift (see Sec. IV).

To further decrease the cost and size of the POP Rb atomic clock, we employ a 100-MHz quartz oscillator ($1.3 \times 10^{-12}/\text{s}$ frequency stability) as the local resonator, whose performance is also plotted in Fig. 8. The quartz oscillator is frequency locked to the central Ramsey fringe by frequency hopping. The error signal is averaged by 3 times to enhance the signal-to-noise ratio. Therefore, the loop feedback cycle is 28.2 ms. Combining the impact from PID parameters, a typical loop bandwidth of approximately 5 Hz is achievable, which ensures that the short-term stability is slightly affected by the quartz oscillator.

IV. NOISE BUDGET FOR LONG-TERM STABILITY

Variation of environmental conditions and aging of components produce low-frequency noises, which deteriorate the long-term stability. Here we quantitatively analyzed the influence of these noise sources on the 40 000

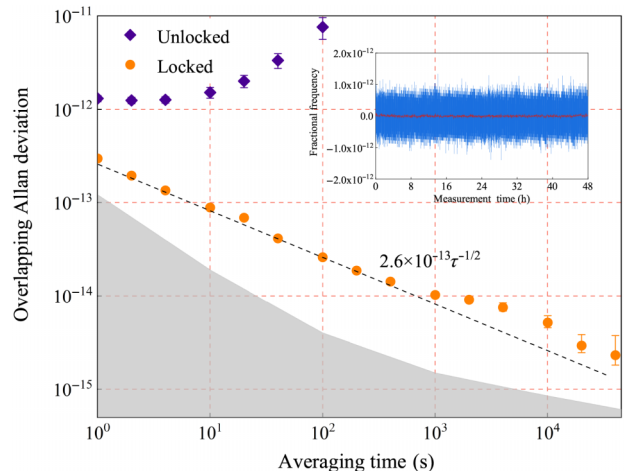


FIG. 8. The overlapping Allan deviation plot, orange disks are the performance of the clock, purple squares are the stability of the quartz crystal oscillator, black dashed line indicates the characteristics of white frequency noise. Error bars correspond to 1σ confidence interval, a linear drift $2.2 \times 10^{-13}/\text{day}$ is subtracted from the data set. The inset is the 48-h record of the fractional frequency with 1-Hz measurement bandwidth (in blue), the data set averaged by 100 times is shown in red.

s frequency stability through different physical effects, as seen in Table I. It should be noted that the physics package is hermetically sealed, so the barometric shift makes negligible contribution to the frequency stability.

A. Zeeman shift

A static magnetic field of 3.5 μT is used to resolve Zeeman-level degeneracy and defines the quantization axis. Zeeman shift for clock transition is expressed as

$$\Delta\nu_z = \frac{(g_J - g_I)^2 \mu_B^2}{2h^2\nu_0} B^2, \quad (5)$$

where g_J and g_I are the Landé g factors of the electron and the nucleus, μ_B the Bohr magneton, h the Planck constant. Three layers of magnetic shields (including the chassis) reduce the contribution of geomagnetism to nT level. The current of Helmholtz coils determines the magnitude of the magnetic field. According to the current fluctuation of the static magnetic at integration time 40 000 s, the magnetic

TABLE I. Frequency stability budget.

Effect	Sensitivity	Fluctuation	Contribution($\times 10^{-15}$)
Zeeman shift	$5.9 \times 10^{-5}/\text{T}$	$7.6 \times 10^{-13}\text{T}$	0.045
Buffer-gas collision	$5.0 \times 10^{-12}/\text{K}$	$1.0 \times 10^{-4}\text{K}$	0.50
Intensity light shift	$5.1 \times 10^{-14}/\%$	0.030%	1.5
Frequency light shift	$2.0 \times 10^{-13}/\text{MHz}$	0.047 MHz	0.94
Cavity-pulling shift	$4.2 \times 10^{-13}/\%$	0.0086%	3.6
Total			4.0

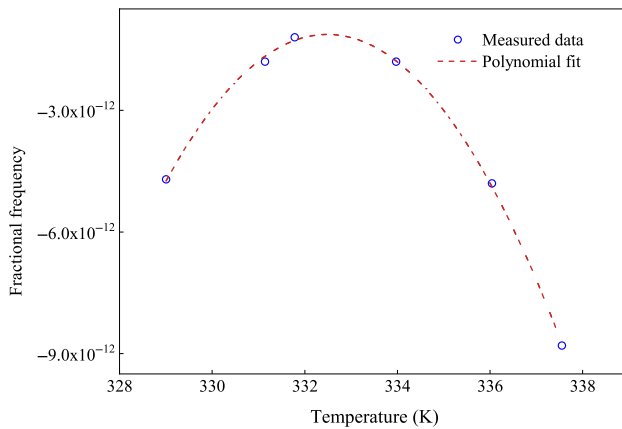


FIG. 9. Clock fractional frequency as a function of the absorption cell temperature.

field variation is 7.6×10^{-13} T, resulting in Zeeman shift contribution of 4.5×10^{-17} .

B. Buffer-gas collision shift

The clock cell is filled with a mixture of Ar and N₂ gases with a pressure of 15 Torr, generating a collision shift of 2771 Hz on the clock transition. The inversion temperature point is measured as 332.5 K, which is shown in Fig. 9. The clock-cell temperature is set within 1 K from the inversion point and we have the temperature coefficient less than $5 \times 10^{-12}/\text{K}$. The environment temperature shows a 0.5-K peak-to-peak variation and 30-mK stability at averaging time of 40 000 s. Thanks to the compact microwave cavity, the sealing physics package, the temperature-compensated baseplate and precision temperature control, the absorption-cell temperature stability is 100 μK . Buffer-gas collision shift contribution to the stability is therefore evaluated to be 5×10^{-16} .

C. Light shift

A pulsed laser is used to create population inversion and probe the atom population. Light shift on the hyperfine levels can be described by

$$\Delta\nu_l(v) = \int_0^\infty S(v)\Phi(v)dv, \quad (6)$$

where $S(v)$ is the light-shift response function and $\Phi(v)$ the photon flux density [41]. Two components contribute to the light shift, the laser intensity, and frequency. Here, we lock the laser frequency to the largest saturated absorption dip $|5S_{1/2}, F=2\rangle \rightarrow |5P_{3/2}, F=2, 3\rangle$ for the best frequency stabilization. The intensity light shift is measured to be $5.1 \times 10^{-14}/\%$. The light shift related to the frequency fluctuation is $2.0 \times 10^{-13}/\text{MHz}$. Laser intensity and frequency contribute a total light shift of 1.8×10^{-15} .

D. Cavity-pulling shift

The cavity-pulling shift is due to the feedback of the microwave cavity on the atoms, which can be described by [42]

$$\Delta\nu_{cp} = \frac{-2Q_L}{T_f v_0} f(\theta, Q_L, T_f) \Delta\nu_c, \quad (7)$$

where Q_L is the loaded quality factor, $\Delta\nu_c$ is the cavity detuning. The microwave pulse area $\theta \propto P^{1/2}T_\mu$, P is the microwave power. Given that the variation of Q_L and $\Delta\nu_c$ due to cavity aging are rather slow over a few days, the frequency shift is mainly caused by microwave-power fluctuation. Besides, in our compact physics package, the microwave cavity and magnetic field coils have similar sizes to the clock cell, which lead to atoms experiencing reduced uniformity of the magnetic and microwave fields. Therefore, we observe more significant microwave-power shift than using a cylindrical standard cavity. The measured microwave-power-shift coefficient is $4.2 \times 10^{-13}/\%$, leading to a corresponding frequency shift of 3.6×10^{-15} .

V. CONCLUSION

We have demonstrated an integrated prototype of the POP Rb clock. The clock exhibits a signal contrast up to 51% and a linewidth of 149 Hz. It presents a short-term frequency stability of $2.6 \times 10^{-13}/\sqrt{\tau}$ and a 40 000 s stability of 2.3×10^{-15} under atmospheric conditions. The volume and power consumption are 23 l and 45 W, respectively. It is worth noting that electronic and optical components account for two thirds of the total volume. Since the cavity-cell assembly is only a few tens of ml, we believe that a size of 2 l is accessible for our atomic clock scheme through optics and electronics integration.

In comparison to the cold-atom clock [7] and ion clock [15], the POP Rb clock has a shorter relaxation time, however, a large number of thermal atoms guarantees comparable frequency stability. The short relaxation time enables a short clock cycle, making an ultrastable local oscillator unnecessary. In addition, the atomic clock presented here operates under atmospheric conditions rather than under ultrahigh vacuum. These features significantly decrease the cost and size, making the proposed clock easily accessible to a wide range of applications.

ACKNOWLEDGMENTS

This work was supported by the Youth Innovation Promotion Association of Chinese Academy of Sciences, and the National Natural Science Foundation of China under Grants No. 2022411 and No. 12173044.

- [1] T. Jennewein, C. Simon, G. Weihs, H. Weinfurter, and A. Zeilinger, Quantum cryptography with entangled photons, *Phys. Rev. Lett.* **84**, 4729 (2000).
- [2] M. A. Fedderke, P. W. Graham, and S. Rajendran, Asteroids for μHz gravitational-wave detection, *Phys. Rev. D* **105**, 103018 (2022).
- [3] H. Ge, B. Li, S. Jia, L. Nie, T. Wu, Z. Yang, J. Shang, Y. Zheng, and M. Ge, Leo enhanced global navigation satellite system (LEGNSS): Progress, opportunities, and challenges, *Geo. Spat. Inf. Sci.* **25**, 1 (2022).
- [4] J. Koelemeij, H. Dun, C. Diouf, E. Dierikx, G. Janssen, and C. Tiberius, A hybrid optical–wireless network for decimetre-level terrestrial positioning, *Nature* **611**, 473 (2022).
- [5] A. A. Belyaev, N. A. Demidov, V. A. Polyakov, and Y. V. Timofeev, Estimation of the possible reduction of the limit frequency instability of a hydrogen generator using an atom beam in one quantum state, *Meas. Tech.* **61**, 779 (2018).
- [6] L. Cacciapuoti, M. Armano, R. Much, O. Sy, A. Helm, M. P. Hess, J. Kehrer, S. Koller, T. Niedermaier, F. X. Esnault *et al.*, Testing gravity with cold-atom clocks in space: The ace-s mission, *Eur. Phys. J. D* **74**, 1 (2020).
- [7] L. Liu, D. Lyu, W. Chen, T. Li, Q. Qu, B. Wang, L. Li, W. Ren, Z. Dong, J. Zhao *et al.*, Inorbit operation of an atomic clock based on laser-cooled ^{87}Rb atoms, *Nat. Commun.* **9**, 2760 (2018).
- [8] Y. Wang, Y. Meng, J. Wan, L. Xiao, M. Yu, X. Wang, X. Ouyang, H. Cheng, and L. Liu, Reaching a few 10^{-15} long-term stability of integrating sphere cold atom clock, *Chin. Opt. Lett.* **16**, 070201 (2018).
- [9] E. Oelker, R. B. Hutson, C. J. Kennedy, L. Sonderhouse, T. Bothwell, A. Goban, D. Kedar, C. Sanner, J. M. Robinson, G. E. Marti, D. G. Matei, T. Legero, M. Giunta, R. Holzwarth, F. Riehle, U. Sterr, and J. Ye, Demonstration of 4.8×10^{-17} stability at 1 s for two independent optical clocks, *Nat. Photonics* **13**, 714 (2019).
- [10] M. Takamoto, I. Ushijima, N. Ohmae, T. Yahagi, K. Kokado, H. Shinkai, and H. Katori, Test of general relativity by a pair of transportable optical lattice clocks, *Nat. Photonics* **14**, 411 (2020).
- [11] P. Yun, F. Tricot, C. E. Calosso, S. Micalizio, B. Francois, R. Boudot, S. Guérardel, and E. de Clercq, High-performance coherent population trapping clock with polarization modulation, *Phys. Rev. Appl.* **7**, 014018 (2017).
- [12] M. A. Hafiz, G. Coget, M. Petersen, C. Rocher, S. Guérardel, T. Zanon, Willette, E. de Clercq, and R. Boudot, Toward a high-stability coherent population trapping Cs vapor-cell atomic clock using autabalanced Ramsey spectroscopy, *Phys. Rev. Appl.* **9**, 064002 (2018).
- [13] C. Perrella, P. Light, J. Anstie, F. Baynes, R. White, and A. Luiten, Dichroic two-photon rubidium frequency standard, *Phys. Rev. Appl.* **12**, 054063 (2019).
- [14] H. Qin, S. Miao, J. Han, N. Xin, Y. Chen, J. Zhang, and L. Wang, High-performance microwave frequency standard based on sympathetically cooled ions, *Phys. Rev. Appl.* **18**, 024023 (2022).
- [15] E. Burt, J. Prestage, R. Tjoelker, D. Enzer, D. Kuang, D. Murphy, D. Robison, J. Seubert, R. Wangs, and T. Ely, Demonstration of a trapped-ion atomic clock in space, *Nature* **595**, 43 (2021).
- [16] S. Micalizio, F. Levi, C. Calosso, M. Gozzelino, and A. Godone, A pulsed-laser Rb atomic frequency standard for GNSS applications, *GPS Solutions* **25**, 94 (2021).
- [17] M. Arditi and T. Carver, Atomic clock using microwave pulse-coherent techniques, *IEEE Trans. Instrum. Meas.*, **2**, 146 (1964).
- [18] A. Godone, S. Micalizio, and F. Levi, Pulsed optically pumped frequency standard, *Phys. Rev. A* **70**, 023409 (2004).
- [19] S. Micalizio, C. E. Calosso, A. Godone, and F. Levi, Metrological characterization of the pulsed Rb clock with optical detection, *Metrologia* **49**, 425 (2012).
- [20] M. Huang, A. Little, and J. Camparo, Lali-pop: Lamp and laser integrated pulsed-optically pumped atomic clock, in *2021 Joint Conference of the European Frequency and Time Forum and IEEE International Frequency Control Symposium (EFTF/IFCS)* (IEEE, Paris, France, 2022), p. 1.
- [21] V. Baryshev, G. Osipenko, A. Novoselov, A. Sukhoverkaya, A. Boyko, and M. Aleynikov, Rubidium frequency standard with pulsed optical pumping and frequency instability of $2.5 \times 10^{-13}/\sqrt{\tau}$, *Quantum Electron.* **52**, 538 (2022).
- [22] E. Batori, C. Affolderbach, M. Pellaton, F. Gruet, M. Violetti, Y. Su, A. K. Skrivelvik, and G. Milet, μPOP clock: A microcell atomic clock based on a double-resonance Ramsey scheme, *Phys. Rev. Appl.* **18**, 054039 (2022).
- [23] D. J. Clark, J. Zacharski, and T. McClelland, Development of a next-generation compact pulsed optically pumped rubidium atomic frequency standard (POPRAFs), in *Proceedings of the 53rd Annual Precise Time and Time Interval Systems and Applications Meeting* (ION, California, USA, 2022), p. 133.
- [24] Q. Shen, H. Lin, J. Deng, and Y. Wang, Pulsed optically pumped atomic clock with a medium- to long-term frequency stability of 10^{-15} , *Rev. Sci. Instrum.* **91**, 045114 (2020).
- [25] Q. Hao, W. Xue, W. Li, F. Xu, X. Wang, W. Guo, P. Yun, and S. Zhang, Microwave pulse-coherent technique-based clock with a novel magnetron-type cavity, *IEEE Trans. Ultrason. Ferroelec. Freq. Contr.* **67**, 873 (2020).
- [26] M. Gozzelino, S. Micalizio, C. E. Calosso, J. Belfi, A. Sapia, M. Gioia, and F. Levi, Realization of a pulsed optically pumped Rb clock with a frequency stability below -15 , *Sci. Rep.* **13**, 12974 (2023).
- [27] G. Mei, F. Zhao, F. Qi, D. Zhong, S. An, P. Wang, G. Ming, F. Wang, Z. Qiu, S. Kang, Q. Wang, H. Wu, S. Yan, L. Hou, C. Wang, and L. Wang, Characteristics of the space-borne rubidium atomic clocks for the BeiDou III navigation satellite system, *Sci. Sin-Phys. Mech. AS.* **51**, 019512 (2021).
- [28] Q. Hao, W. Xue, F. Xu, K. Wang, P. Yun, and S. Zhang, Efforts towards a low-temperature-sensitive physics package for vapor cell atomic clocks, *Satell. Navig.* **1**, 43 (2020).
- [29] W. Moreno, M. Pellaton, C. Affolderbach, and G. Milet, Barometric effect in vapor-cell atomic clocks, *IEEE Trans. Ultrason. Ferroelec. Freq. Contr.* **65**, 1500 (2018).

- [30] J. Vanier, R. Kunski, N. Cyr, J. Y. Savard, and M. Têtu, On hyperfine frequency shifts caused by buffer gases: Application to the optically pumped passive rubidium frequency standard, *J. Appl. Phys.* **53**, 5387 (1982).
- [31] O. Kozlova, S. Guérardel, and E. de Clercq, Temperature and pressure shift of the Cs clock transition in the presence of buffer gases: Ne, N₂, Ar, *Phys. Rev. A* **83**, 062714 (2011).
- [32] W. Li, Q. Hao, Y. Du, S. Huang, P. Yun, and Z. Lu, Demonstration of a sub-sampling phase lock loop based microwave source for reducing dick effect in atomic clocks, *Chinese Phys. Lett.* **36**, 070601 (2019).
- [33] G. J. Dick, Local oscillator induced instabilities in trapped ion frequency standards, in *Proceedings of the 19th Annual Precise Time and Time Interval Systems and Applications Meeting* (ION, California, USA, 1987), p. 133.
- [34] R. H. Dicke, The effect of collisions upon the Doppler width of spectral lines, *Phys. Rev.* **89**, 472 (1953).
- [35] J. Vanier and C. Mandache, Ramsey-fringe shape in an alkali-metal vapor cell with buffer gas, *Appl. Phys. B* **87**, 565 (2007).
- [36] J. Vanier, J. F. Simard, and J. S. Boulanger, Relaxation and frequency shifts in the ground state of Rb⁸⁵, *Phys. Rev. A* **9**, 1031 (1974).
- [37] W. Franzen, Spin relaxation of optically aligned rubidium vapor, *Phys. Rev.* **115**, 850 (1959).
- [38] M. Gozzelino, S. Micalizio, C. E. Calosso, A. Godone, and F. Levi, Kr-based buffer gas for Rb vapor-cell clocks, *IEEE Trans. Ultrason. Ferroelec. Freq. Contr.* **68**, 1442 (2021).
- [39] S. Micalizio, C. E. Calosso, F. Levi, and A. Godone, Ramsey-fringe shape in an alkali-metal vapor cell with buffer gas, *Phys. Rev. A* **88**, 033401 (2013).
- [40] S. Kang, M. Gharavipour, C. Affolderbach, F. Gruet, and G. Mileti, Demonstration of a high-performance pulsed optically pumped Rb clock based on a compact magnetron-type microwave cavity, *J. Appl. Phys.* **117**, 104510 (2015).
- [41] W. Happer, Optical pumping, *Rev. Mod. Phys.* **44**, 169 (1972).
- [42] M. Gozzelino, S. Micalizio, F. Levi, A. Godone, and C. E. Calosso, Reducing cavity-pulling shift in Ramsey-operated compact clocks, *IEEE Trans. Ultrason. Ferroelec. Freq. Contr.* **65**, 1294 (2018).